How to Cite: Soualmi, S., Henni, M., Djahnit, L., & Bouzegaou, M. (2025). Structural, Photocatalytic, and Antibacterial Evaluation of Cu-Doped $ZnMn_2O_4$ Nanoparticles. *Eurasian Journal of Chemistry.* https://doi.org/10.31489/2959-0663/4-25-3

Article

Received: 6 June 2025 | Revised: 27 October 2025 |
Accepted: 10 November 2025 | Published online: 26 November 2025

UDC 546.02+544.42

https://doi.org/10.31489/2959-0663/4-25-3

Saida Soualmi[1*], Meriem Henni[1], Leila Djahnit[2,3], Maroua Bouzegaou[1]

[1]*Laboratory of Synthesis and Catalysis, University of Ibn Khaldoun Tiaret, Tiaret, Algeria;*
[2]*Chemistry Department, Faculty of Exact Sciences and Informatics, University Hassiba Benbouali Chlef (UHBC), Chlef, Algeria;*
[3]*Renewable Energy and Materials Laboratory, University of Medea, Medea, Algeria*
*(*Corresponding author's e-mail: saida.soualmi@univ-tiaret.dz)*

Structural, Photocatalytic, and Antibacterial Evaluation of Cu-Doped $ZnMn_2O_4$ Nanoparticles

In this study, the impact of doping $ZnMn_2O_4$ spinel nanoparticles with different proportions of copper (Cu) was investigated for the first time. The nanomaterials were synthesized via sol-gel method and characterized structurally, optically, and morphologically. X-ray diffraction (XRD) confirmed the formation of a pure tetragonal spinel phase, with no secondary phases detected. Successful incorporation of Cu^{2+} ions into the $ZnMn_2O_4$ lattice was confirmed by shifts in peak positions and intensities. FTIR analysis revealed distinct Zn–O and Mn–O vibrations, confirming the structural integrity of the spinel. The optical band gap, estimated via Tauc plots, decreased from 2.61 eV for undoped $ZnMn_2O_4$ to 1.58 eV for 3 % Cu-doped samples, indicating improved light absorption properties. SEM analysis showed that Cu doping induced increased porosity and particle agglomeration. Photocatalytic activity was evaluated through the degradation of Methylene Blue under visible light; notably, the sample with 1 % Cu achieved an efficiency of 87.7 %. Furthermore, the doped nanoparticles exhibited strong antibacterial activity against both Gram-positive and Gram-negative bacteria, with pronounced inhibition observed against *E. coli*. These findings highlight the multifunctionality of Cu-doped $ZnMn_2O_4$ for environmental and biomedical applications.

Keywords: spinel, synthesis, nanomaterials, photocatalysis, doping, antibacterial, sol-gel, copper

Introduction

Nanoparticles have become an interesting research focus in various environmental fields. Their effectiveness has been demonstrated in drug delivery, antibacterial activity [1, 3], and gas sensors [4]. Among these nanomaterials, nickel-and copper-doped $ZnMn_2O_4$, which can address current energy, health, and environmental challenges. $ZnMn_2O_4$ is a promising material due to its electrical, optical, and catalytic properties. These intrinsic characteristics can be further improved by the incorporation of dopants such as Bi, Al, and Mg. In a study conducted by Heba et al. [5], Sn-doped $ZnMn_2O_4$ showed notable improvements in structural and optical properties. According to Heba [6], spinels based on $ZnMn_2O_4$ were synthesized using the sol-gel method and doped with Bi^{3+} ions. They successfully enhanced the material's functional properties for applications in optoelectronics. A recent study on the influence of aluminum doping on the structural, optical, and electrical characteristics of $ZnMn_2O_4$ was conducted by Heiba et al. [7]. They found that aluminum doping significantly alters the structural, optical, and electrical properties of $ZnMn_2O_4$. The $Zn_{1-x}Al_xMn_2O_4$ compounds were synthesized through an atomic layer drying thermal treatment. The effect of doping with Al^{3+} ions on the crystalline structure and electrochemical properties was studied [8].

Rajesh et al. [9] demonstrated that doping the spinel $CdAlO_4$ with Zn increases its photocatalytic efficiency. To examine the effect of doping, Ma et al. [10] synthesized $ZnMn_2O_4$ nanocrystals doped with Co^{2+} using a hydrothermal technique. They found that the photocatalytic activity of doped $Zn_{1-x}Co_xMn_2O_4$ sam-

ples was significantly higher than that of pure $ZnMn_2O_4$ samples for the photodegradation of methyl orange (MO) under visible light irradiation.

This study aims to investigate the photocatalysis of Methylene Blue (MB)using pure and doped $ZnMn_2O_4$ nanoparticles with Cu and their antibacterial activity against E. coli and S. aureus bacteria. This research introduces, for the first time, Cu-doped $ZnMn_2O_4$ Nanoparticles to study their photocatalytic Performance, and Antibacterial Properties.

Experimental

Materials

Zinc nitrate hexahydrate ($Zn(NO_3)_2 \cdot 6H_2O$) was purchased from Panreac, 99 % purity. Manganese (II) nitrate $Mn(NO_3)_2 \cdot 4H_2O$ obtained from Fluka ≥ 98 % purity. Copper (II) nitrate trihydrate $Cu(NO_3)_2 \cdot 3H_2O$ obtained from Biochem, Citric acid $C_6H_8O_7$ obtained from Biochem and Methylene blue (Merck chemicals).

Synthesis of Copper doped $ZnMn_2O_4$ Nanoparticles

A facile sol–gel method was used to synthesize pure and Cu-doped $ZnMn_2O_4$ nanoparticles. A mixture 0.0052 mol of zinc nitrate hexahydrate ($Zn(NO_3)_2 \cdot 6H_2O$) and 0.01 mol of manganese (II) nitrate tetrahydrate ($Mn(NO_3)_2 \cdot 4H_2O$) were dissolved in 100 mL of deionized water. The two solutions were then mixed with vigorous agitation at room temperature for 30 minutes to ensure homogeneity. Citric acid, used as a complexing agent, as well as $Cu(NO_3)_2 \cdot 3H_2O$ (0.0376 g) dissolved in ethanol, were successively added to the reaction mixture. The solution was then heated and stirred at 90 °C until the gel was formed then converted into a powder, which was dried in an oven at 70 °C for 24 hours. Finally, the dried powder was calcined at 600 °C for 4 hours, resulting in the formation of $ZnMn_2O_4$ nanocomposites, as illustrated in Scheme 1.

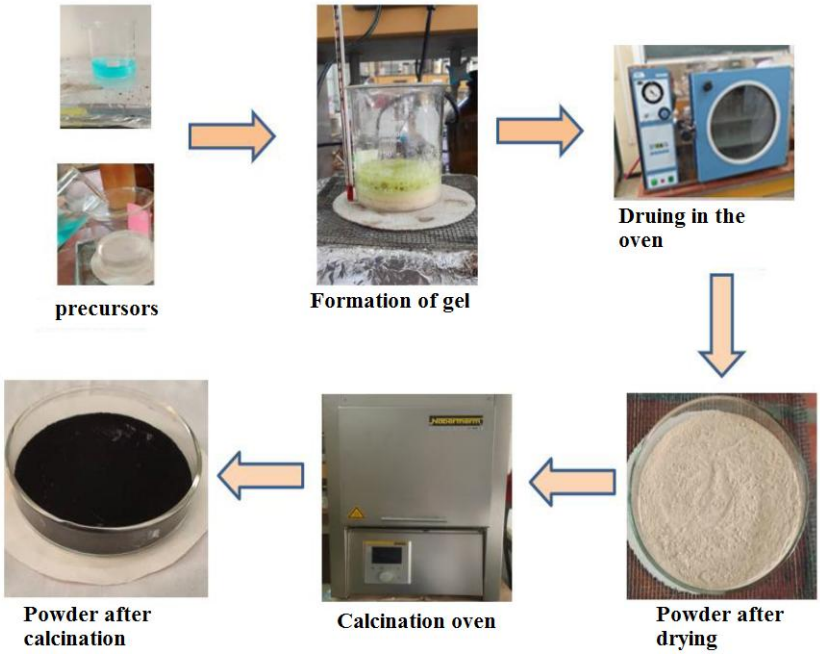

Scheme 1. Spinel synthesis protocol

Antibacterial Activity

Preparation of the Bacterial Suspension

The evaluation of the antibacterial activity of the prepared nanoparticles was carried out on both Gram-negative and Gram-positive bacteria, namely *Escherichia coli* ATCC 25922, *Bacillus subtilis* ATCC 6633, *Staphylococcus aureus* ATCC 25925, and *Bacillus cereus* ATCC 10876. The strains were cultured at 37 °C in Mueller Hinton medium for 24 hours. The bacterial culture was adjusted to 0.5 McFarland standard using a spectrophotometer set at a wavelength of 625 nm, with an optical density (OD) ranging between 0.08 and 0.1, corresponding to approximately 1×10^8 CFU/mL [11].

Agar Well Diffusion Method

The agar well diffusion method, adapted from Imran et al. [12], was used to evaluate the antimicrobial activity of the oxide nanoparticles, with some modifications. Culture plates were prepared using sterilized Mueller-Hinton agar. One milliliter of the bacterial suspension was evenly spread over the agar surface. Each Petri dish was perforated with four wells, each 6 mm in diameter. Then, 100 µL of each nanoparticle (NP) concentration (10 mg/mL, 15 mg/mL) was added to the wells. The positive control was performed using the antibiotic Piperacillin PRL100 (100 µg). The plates were incubated at 37 °C for 24 hours. Finally, antimicrobial potency was determined by measuring the inhibition zones in millimeters using a caliper.

Characterization

Characterization of the synthesized nanocomposites' properties was carried out using X-ray diffraction (XRD, Rigaku MINIFLEX 600) using Cu Kα radiation (λ = 1.5406) and a scanning rate of 5° min^{-1}. Perkin Elmer Spectrum One FTIR was used to analyze the samples following KBr pellets, in the range of 4000–400 cm^{-1}. A QUANTA 650 FEI scanning electron microscopy (SEM) was used to examine the morphology of the produced spinel oxides.

Results and Discussion

FT-IR Spectra

FTIR spectra of $ZnMn_2O_4$ samples (Fig. 1), whether undoped or doped with 1 % and 3 % copper (Cu) were analyzed. Strong signals were detected from 400 to 600 cm^{-1} related to the vibrations of the metal-oxygen M–O bond. Bands of the octahedral Zn–O and tetrahedral Mn–O groups were observed around 400 and 600 cm^{-1}, respectively.

These observations, in line with those of Roya et al. [13], confirm that the inverse spinel structure of $ZnMn_2O_4$, with Zn^{2+} in the tetrahedral sites and Mn^{3+} in the octahedral sites, has indeed been achieved.
The O-H stretching vibration peaks between 3400 to 3200 cm^{-1} were detected in the spectrum due to surface water and hydroxyl group presence. A band present at 1630 cm^{-1} indicates either H–O–H bending or C=O stretching although it points toward the existence of surface water or hydroxyl groups typical for aqueous precipitation materials. A band at 1380 cm^{-1}, probably due to symmetric deformation vibrations of CH_3 groups, indicated the presence of organic residues, likely from citric acid used as a chelating agent. Moreover, bands at 995 cm^{-1} (ν(C–O) vibrations or NO_3^- nitrates) and 878 cm^{-1} (out-of-plane deformation of COO^- carboxylates) revealed that an incomplete calcination of the precursors occurred.

FTIR analysis clearly demonstrates that doping significantly affects the intensity of the bands. When copper is added up to 3 %, there is a notable increase in intensity, indicating that Cu^{2+} ions are properly integrated into the crystal lattice. On the other hand, the intensity decreases when the content reaches 6 %, indicating that the structure begins to be disturbed or saturated. This destabilization may be related to the fact that the radius of ionized Cu^{2+} (0.73) is marginally larger than that of Mn^{2+} (0.65), which leads to internal stresses in the highly concentrated lattice. This may be due to the slightly larger ionic radius of Cu^{2+} compared to that of Mn^{2+}, which introduces high concentration stresses in the lattice.

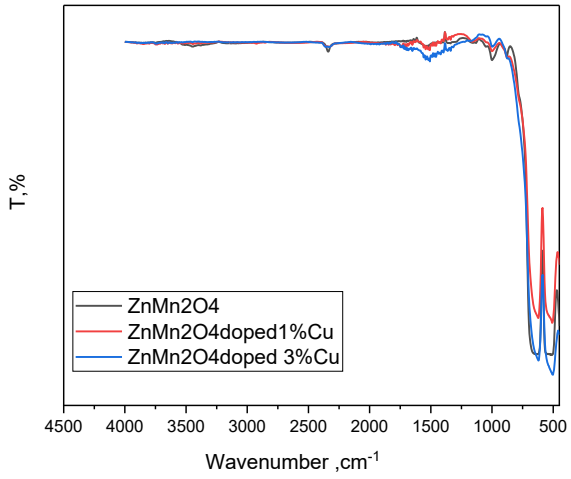

Figure1 FTIR absorption spectra of all Cu-doped $ZnMn_2O_4$ compounds

XRD Measurements

X-ray diffraction (XRD) analysis (Figure 2) confirmed the formation of the $ZnMn_2O_4$ spinel structure (heterolite) for all samples, both doped and undoped, in accordance with JCPDS card no. 96-901-2843. The diffraction peaks observed at 2θ values of 18.224°, 29.39°, 31.23°, 33.09°, 36.40°, 50.58°, 52.11°, 54.41°, 59.1°, 60.82°, and 65.16° correspond well to the (011), (112), (020), (013), (121), (220), (015), (132), (231), (224), and (040) crystallographic planes, respectively. The undoped sample exhibited no additional or secondary peaks, confirming its phase purity and high crystallinity.

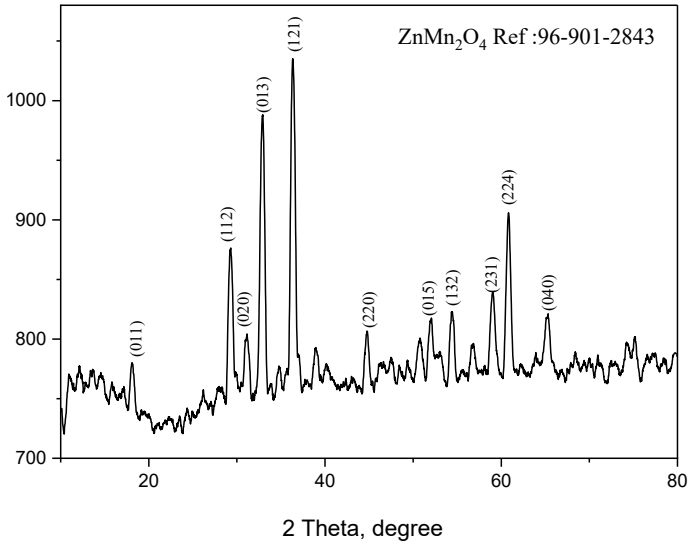

Figure 2. XRD spectrum of $ZnMn_2O_4$ nanocomposite

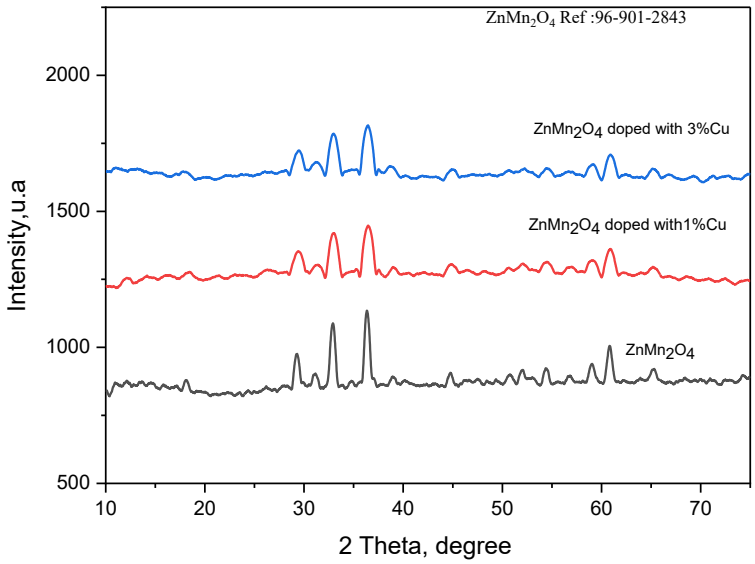

Figure 3. XRD spectrum of Cu-doped $ZnMn_2O_4$ nanocomposite

The diffraction peaks are perfectly indexed to the $ZnMn_2O_4$ phase of inverse spinel type (heterolite structure), referenced to the data of JCPDS card no. 96-901-2843. As shown in Figure 3, increasing the Cu doping level from 1 % to 3 % induces noticeable changes in peak positions and intensities. In comparison with the undoped material, the sample containing 1 % Cu. However, when the Cu content is increased to 3 %, the structural changes become more evident. This suggests that a higher Cu concentration leads to increased lattice strain and possible distortions within the crystal framework, likely due to the integration of Cu^{2+} ions into the lattice. Alongside these effects, a gradual rise in crystallite size was also noticed with increasing Cu levels, indicating that Cu^{2+} may play a role in promoting or facilitating crystal growth.

The average crystallite size of spinel grains (Table I) was calculated by the Debye–Scherrer equation applied to the most intense diffraction line [14]:

$$D_c = \frac{K\lambda}{\beta cos\theta},$$

where $K = 0.9$; D — is the catalyst's crystallite size; λ — is the X-ray wavelength; β — is the "Full Width at Half Maximum (FWHM)"; θ — is the diffraction angle.

Table 1

The average crystallite size of the synthesized spinels

Sample	Crystallite size D (nm)
$ZnMn_2O_4$	24.82
$ZnMn_2O_4$doped with 1 %Cu	30.21
$ZnMn_2O_4$doped with3 %Cu	32.82

Optical Band Gap of the Synthesized Spinels

The optical band gap is a physical property that corresponds to the energy difference between the valence band and the conduction band. The determination of the band gap energy was carried out using a reflectance method based on Tauc's theory [15].

The calculation of Eg was performed using Tauc's equation.

$$\alpha_{h\upsilon} = \alpha_0(h\upsilon - E_g)^{1/2},$$

where — α_0 is a constant, E_g is the band gap energy, α — is the absorption coefficient given by $\alpha = 2.303 A/d$; there d — is the thickness of the sample (in our case, the cuvette thickness d is 1 cm), A — is the absorbance, $h\upsilon$ — is the photon energy, hence: $h\upsilon$(eV) = 1240/λ, were λ — is the incident wavelength (nm)

In the course of this study, the optical band gap was estimated to be around 2.61 eV (Figure 4). This value is fairly consistent with what has been previously reported in the literature — 2.49 eV in reference [16] with only a slight difference of 0.12 eV, which falls within the expected margin of experimental error. Similarly, the absorption wavelength recorded here (475 nm) is close to the previously cited value of 498 nm [16], supporting the idea that the material absorbs within the UV-visible range. Figures 4 to 6 show the Tauc plots corresponding to both the undoped and Cu-doped $ZnMn_2O_4$ samples. A clear reduction in the band gap is observed as more copper is introduced: it drops from 2.61 eV in the pure sample to 1.77 eV and 1.58 eV for the 1 % and 3 % Cu-doped materials, respectively.

This trend agrees with what has been highlighted in earlier works [17], where doping is known to affect the electronic structure of metal oxides often by narrowing the band gap due to the introduction of new energy levels or changes within the lattice.

The band gap narrows mainly because copper ions create new energy levels within it. These extra levels let electrons move between states more easily, requiring less energy and thus reducing the overall optical band gap This phenomenon comes from the interaction between the Cu 3*d* orbitals and the electronic structure of the host oxide—a mechanism that has been widely observed in other transition metal oxides like ZnO and CuO [18]. Additionally, the narrowing of the band gap in Cu-doped $ZnMn_2O_4$ can also be influenced by structural defects and the interactions between copper and manganese ions, which together modify the electronic environment of the material. Similar patterns have been reported in copper-doped ZnO, TiO_2 [19], and other spinel oxides doped with Cu [20]. Interestingly, the band gap reduction is more noticeable in $ZnMn_2O_4$, likely because of the distinctive electronic characteristics of manganese-based spinels.

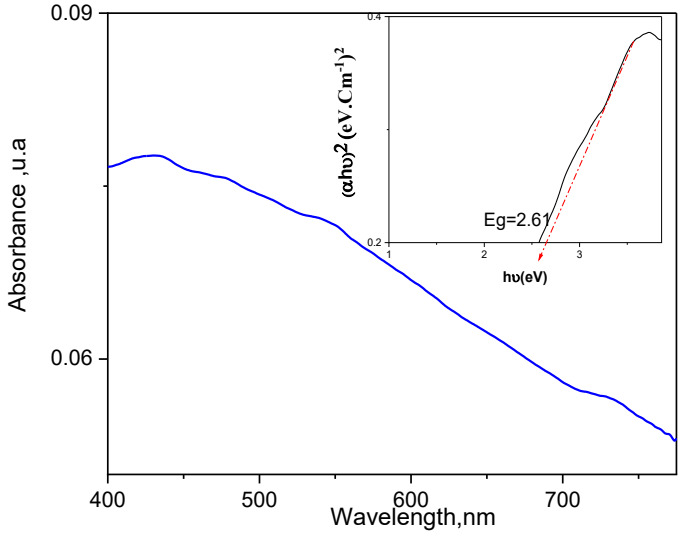

Figure 4. Tauc plots of $ZnMn_2O_4$ nanoparticles

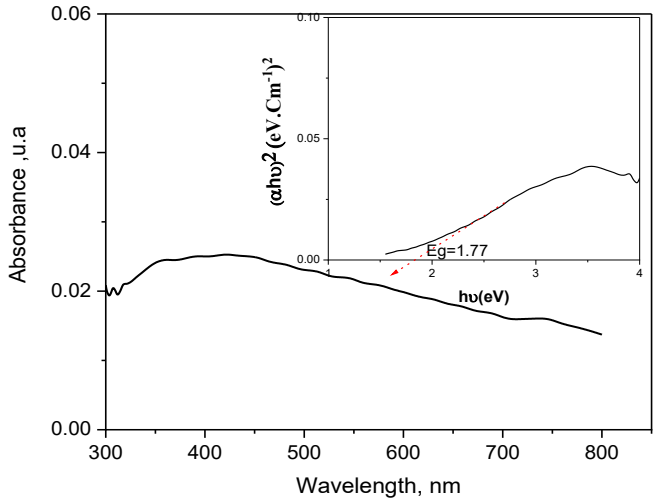

Figure 5. Tauc plots of $ZnMn_2O_4$ NPs doped with 1 % Cu

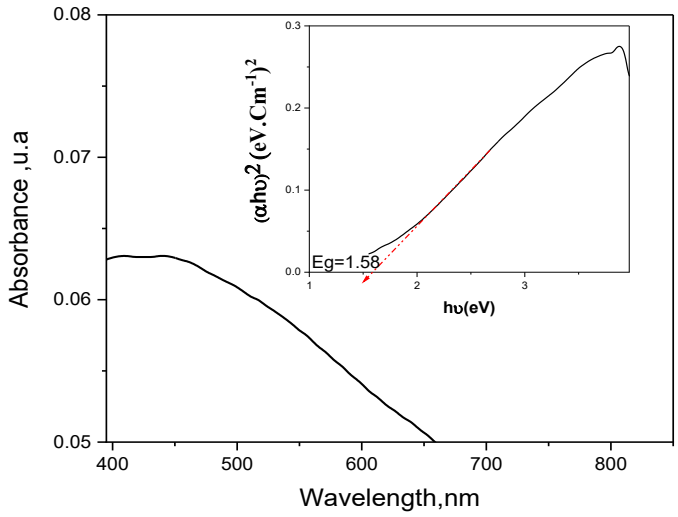

Figure 6. Tauc plots of $ZnMn_2O_4$ NPs doped with 3 % Cu

Scanning Electron Microscopy (SEM)

The morphology of the 3 % Cu-doped $ZnMn_2O_4$ nanoparticles, observed by scanning electron microscopy (SEM) and shown in Figure 7, reveals a heterogeneous porous structure. The pore sizes range roughly from 50 to 200 nm, as estimated using the 2 μm scale bar. The morphology consists of a complex three-dimensional network formed by spheroidal or irregular particles that tend to agglomerate into porous assemblies. Such elevated porosity is characteristic of materials engineered for applications requiring a high specific surface area, including gas sensing and battery electrodes. In the first case (Fig. 7*a*), the surface is rough and porous, characterized by irregular aggregates of angular particles, indicating a marked influence of Cu doping on pore density and distribution. In contrast, in Fig. 7*b*, the texture appears more homogeneous, with regularly distributed spheroidal or lamellar particles, suggesting a structured organization in layers or stacking. Finally, Fig. 7*c* highlights a complex mixed morphology, dominated by well-developed porosity.

The pronounced porosity and clustering in the Cu-doped samples probably result from copper's impact on how the crystals grow, causing the particles to stick together more easily. Since the ionic sizes of Cu^{2+} (73 pm), Zn^{2+} (74 pm), and Mn^{3+} (65 pm) are quite close, copper ions can replace either zinc or manganese in the crystal lattice. When copper ions take the place of others in the lattice, they can create defects that promote the formation of a porous structure. In contrast, doping with tin usually leads to dense, angular particles with very little porosity [21], making it quite different from the more open, porous structure seen with copper doping. Cobalt doping falls somewhere in between, leading to particles that are mostly round with less porosity [9]. These differences clearly show how important the choice of dopant is in shaping $ZnMn_2O_4$ nanoparticles: copper encourages a highly porous structure, cobalt results in moderate aggregation with smoother particles, and tin creates a denser, more compact material.

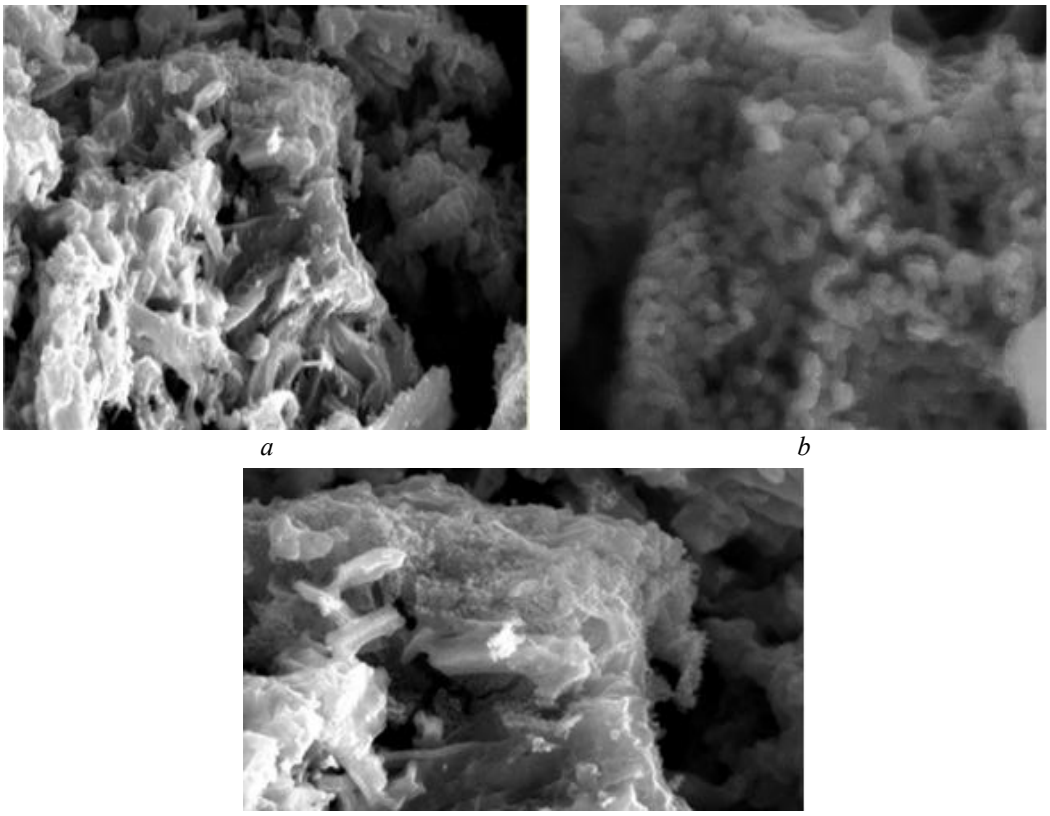

a *b* *c*

Figure 7. SEM micrographs profile of Cu-doped $ZnMn_2O_4$. The images show (*a*) rough, porous surface with irregular angular aggregates; (*b*) a more homogeneous texture with regularly distributed spheroidal or lamellar particles suggesting structured layering; (*c*) a complex mixed morphology with high overall porosity (pore sizes ranging from 50 to 200 nm, scale bar = 2 μm

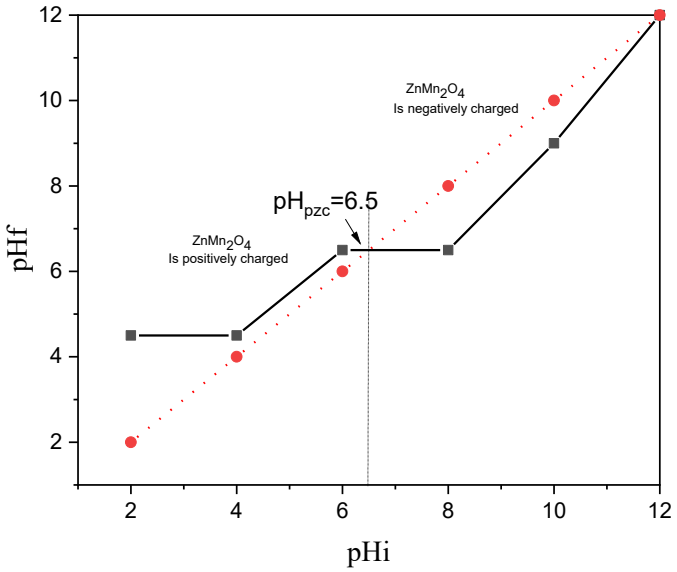

Figure 8. Determination of the pH_{pzc} for $ZnMn_2O_4$

Photocatalysis

The point of zero charge (pHpzc) was determined using the pH drift method [22]. The pHpzc is equal to 6.5 (Figure 8) was identified as the intersection point between the final pH versus initial pH curve and the line $pH_{final} = pH_{initial}$.

The photodegradation of Methylene Blue (MB) dye by synthesized $ZnMn_2O_4$ spinels, both undoped and copper-doped, using a 30 W visible light source, was investigated. Figure 9 shows the photocatalytic degradation of MB by $ZnMn_2O_4$ synthesized at pH 12, where a significant adsorption of the dye is observed over time (adsorption equilibrium reached before irradiation). After irradiation, a gradual decrease in the intensity of the absorption peak at 664 nm is observed over time (from 30 to 180 minutes), with a degradation rate of 71.71 %, which is a good yield, especially for a dye that is difficult to degrade. As shown in Figure 10, $ZnMn_2O_4$ doped with 3 % Cu reached a degradation efficiency of 78.21 %. Notably, the sample doped with 1 % Cu exhibited the highest photocatalytic performance, with a degradation rate of 87.7 % (Figure 11). This enhancement can be attributed to the beneficial role of copper in promoting charge carrier separation and introducing favorable structural defects.

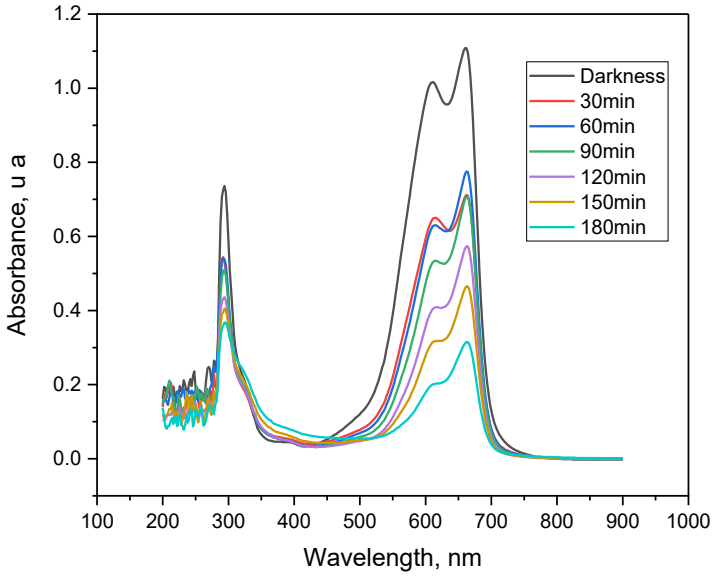

Figure 9. Photocatalytic degradation of Methylene Blue (MB) by synthesized $ZnMn_2O_4$, with MB concentration of 0.01g/L and $ZnMn_2O_4$ concentration of 0.1 g/L

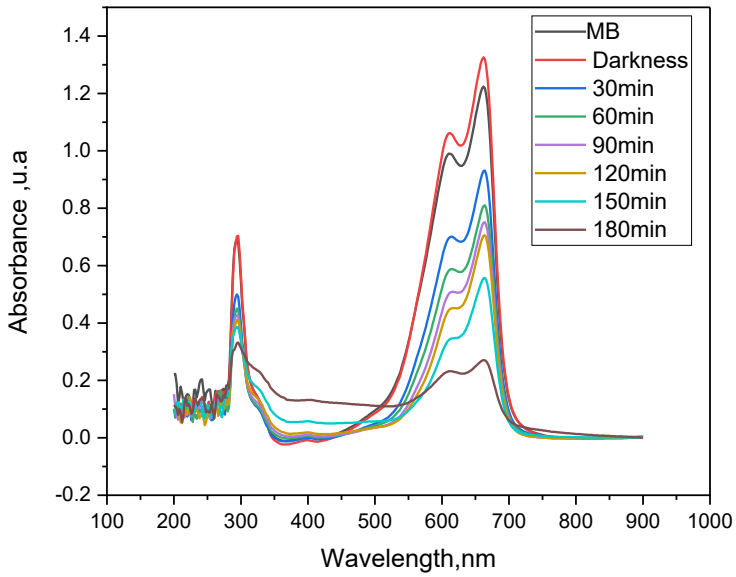

Figure 10. Photocatalytic degradation of Methylene Blue (MB) by 3 % Cu-doped $ZnMn_2O_4$, synthesized with an MB concentration of 10 mg/L and a 1 % Cu-doped $ZnMn_2O_4$ concentration of 0.1 g/L

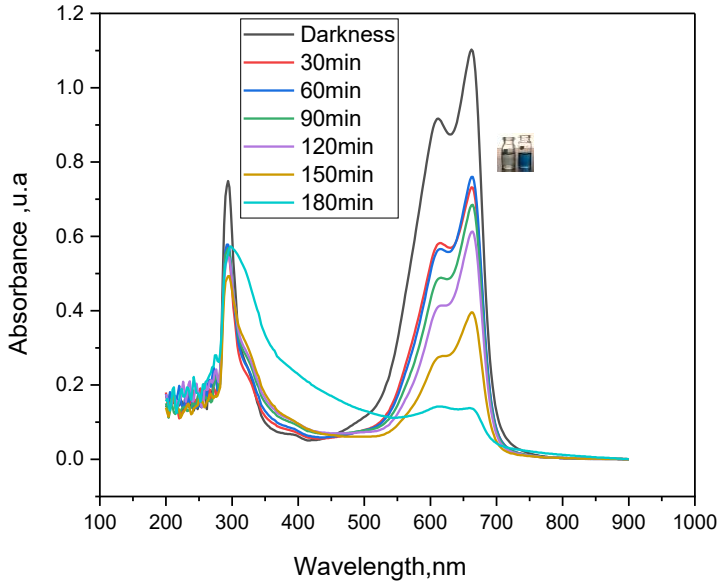

Figure 11. Photocatalytic degradation of Methylene Blue (MB) by 1 % Cu-doped $ZnMn_2O_4$, synthesized with an MB concentration of 0.01g/L and a 1 % Cu-doped $ZnMn_2O_4$ concentration of 0.1 g/L

Antibacterial Activity

The antibacterial activity results of the synthesized $ZnMn_2O_4$ nanoparticles, both doped and undoped, revealed notable antibacterial effects against all tested strains. The inhibition zones around the wells are shown in Figures 12, 13, 14, and 15, and the measured inhibition values are presented in Table 2.

It was observed that the antibacterial activity of Cu-doped nanoparticles is higher compared to undoped nanoparticles. Figure 12 confirms that the synthesized nanoparticles effectively inhibit the growth of *Bacillus subtilis*, producing inhibition zones ranging from 10 to 14 mm. In contrast, the standard antibiotic showed a considerable inhibition zone of 27 mm.

Each sample exhibited a moderate inhibition zone against the *S. aureus* strain, with diameters ranging from 11 to 15 mm, similar to that of the antibiotic (Figure 13). However, the various nanoparticles demonstrated significant antibacterial properties against the *Bacillus cereus* strain, with inhibition zones ranging from 10 to 14 mm (Figure 14). In comparison, the standard antibiotic exhibited a strong inhibition zone of

29 mm. These findings confirm that increasing the concentration of pure and doped nanoparticles is associated with enhanced inhibition of bacterial growth.

Regarding *E. coli* bacteria, as shown in Figure 15, all nanoparticles demonstrated notable antibacterial activity, with inhibition zones ranging from 10 to 16 mm. In contrast, the standard antibiotic showed a significant inhibition zone of 25 mm. Figure 16 clearly shows the expansion of the inhibition zone with the increase in nanoparticle concentration and doping percentage.

In other studies, Soualmi al. also confirmed that $ZnMn_2O_4$ nanoparticles showed strong antibacterial activity against *E. coli*, *S. aureus*, *B. cereus*, and *B. subtilis* [2].

However, the Cu-doped nanoparticles exhibited a notable inhibitory effect against all strains, with a particularly large inhibition zone observed against *E. coli*. Therefore, doping with copper proved to be more effective against *E. coli* (Gram-negative) than against *S. aureus* (Gram-positive). These results are consistent with the findings of Bogdanovi et al., who demonstrated that *E. coli* strains are generally more sensitive to copper nanoparticles compared to *S. aureus* [22].

According to Giannousi et al., copper nanoparticles (Cu-NPs) and copper oxide (Cu_2O) exhibit strong antibacterial properties, notably by inducing plasmid DNA degradation in a dose-dependent manner across both Gram-positive and Gram-negative bacteria [23]**.** In addition, the antibacterial action of ZnO and CuO nanoparticles is generally thought to result from the release of Cu^{2+} and Zn^{2+} ions, which tend to bind to the negatively charged surfaces of bacterial cells [24].

This interaction may disrupt biochemical processes and damage cell membranes. Additionally, the small size of the nanoparticles facilitates their attachment to the bacterial cell wall, leading to cell destruction. Nanoparticles capable of damaging essential bacterial enzymes may also penetrate the cell membrane [25, 26].

Table 2

Diameter of inhibition zones against microorganisms

Bacteria	Zone of inhibition (mm)						
	Control	$ZnOMn_2O_4$		$ZnOMn_2O_4$-Cu 1 %		$ZnOMn_2O_4$-Cu 3 %	
		10 mg/ml	15 mg/ml	10 mg/ml	15 mg/ml	10 mg/ml	15 mg/ml
Bacillus cerus	25	10	12	12	13	13.5	14
Escherichia coli	23	10	11.5	11	14.5	14	16
Staphylococus aureus	13	11	12	12	14	13	15
Bacillus subtilis	27	11.5	13	12	13	12.5	14

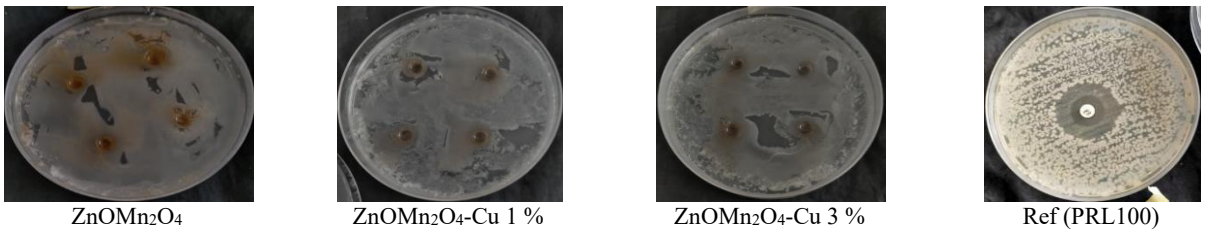

$ZnOMn_2O_4$ $ZnOMn_2O_4$-Cu 1 % $ZnOMn_2O_4$-Cu 3 % Ref (PRL100)

Figure 12. Results of antibacterial activity against *Bacillus subtilis*

$ZnOMn_2O_4$ $ZnOMn_2O_4$-Cu 1 % $ZnOMn_2O_4$-Cu 3 % Ref (PRL100)

Figure 13. Results of antibacterial activity against *S. Aureus*

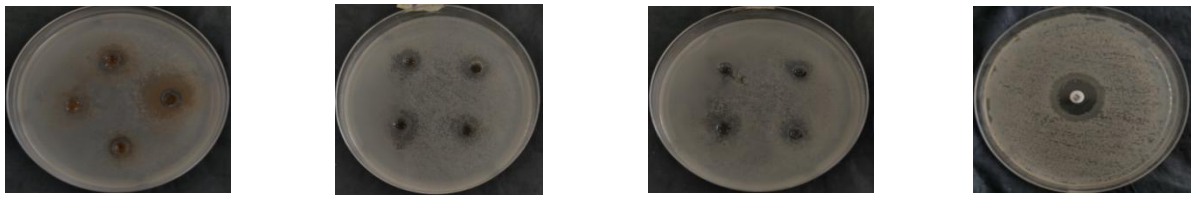

$ZnOMn_2O_4$ $ZnOMn_2O_4$-Cu 1 % $ZnOMn_2O_4$-Cu 3 % Ref (PRL100)

Figure 14. Results of antibacterial activity against *Bacillus Cereus*

$ZnOMn_2O_4$ $ZnOMn_2O_4$-Cu 1 % $ZnOMn_2O_4$-Cu 3 % Ref (PRL100)

Figure 15. Results of antibacterial activity against *E. Coli*

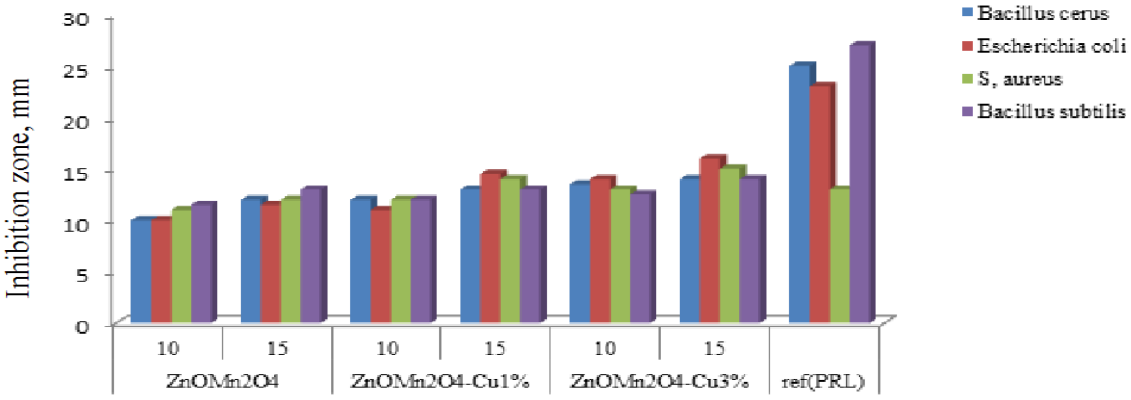

Figure 16. Antibacterial effects of nanoparticles

Conclusions

The effect of incorporating different amounts of copper (Cu) into $ZnMn_2O_4$ spinel nanoparticles was investigated in this study for the first time. A sol-gel method was used to synthesize the nanoparticles, followed by their structural, optical, and morphological characterization. FTIR results confirmed that the material possesses a spinel structure, as evidenced by bands located between 400 and 600 cm^{-1}. Copper doping increased band intensity, indicating successful incorporation without altering the main structure. The results of SEM are typical of materials produced through methods like co-precipitation or hydrothermal synthesis [27].

The presence of copper seemed to promote noticeable particle agglomeration and increased surface roughness features often associated with crystalline imperfections which could enhance performance in applications requiring a large specific surface area. The best photocatalytic performance was shown by $ZnMn_2O_4$ doped with 1 % copper, which achieved 87.7 % MB degradation, attributed to improved charge separation and structural defects. $ZnMn_2O_4$ nanoparticles exhibit notable antibacterial activity against *B. cereus*, *E. coli, S. aureus* and *B. subtilis* strains. However, copper-doped nanoparticles, specifically $ZnMn_2O_4$,3 %, exhibit better antibacterial properties. Overall, these results demonstrate that controlled copper doping not only preserves the spinel structure of $ZnMn_2O_4$ nanoparticles but also enhances their photocatalytic and antibacterial activity, highlighting their potential for environmental and biomedical applications.

*Author Information**

**The authors' names are presented in the following order: First Name, Middle Name and Last Name*

Saida Soualmi (*corresponding author*) — Doctor and Researcher, Laboratory of Synthesis and Catalysis, University of Ibn Khaldoun Tiaret, 14000, Tiaret, Algeria; e-mail: saida.soualmi@univ-tiaret.dz; https://orcid.org/0009-0009-4858-8695

Meriem Henni — Doctor and Researcher, Laboratory of Synthesis and Catalysis, University of Ibn Khaldoun Tiaret, 14000, Tiaret, Algeria; e-mail: hanan1112@yahoo.fr, https://orcid.org/0009-0005-5378-0674

Leila Djahnit — Doctor and Researcher, Chemistry Department, Faculty of Exact Sciences and Informatics, University Hassiba Benbouali Chlef (UHBC), 02000, Chlef, Algeria; Renewable Energy and Materials Laboratory, University of Medea, 26000, Medea, Algeria; e-mail: Leila_djahnit@yahoo.fr, https://orcid.org/0000-0001-5834-8024

Maroua Bouzegaou — Master Student, Chemistry Department, Laboratory of Synthesis and Catalysis, University of Ibn Khaldoun Tiaret, 14000, Tiaret, Algeria; e-mail: bouzegaoumaroua3@gmail.com

Author Contributions

The manuscript was written through contributions of all authors. All authors have given approval to the final version of the manuscript. CRediT: **Saida Soualmi** conceptualization, data curation, investigation, methodology, validation, visualization, writing-review & editing, interpreted the results, plotted the graphs, and wrote the manuscript performed the photocatalytic degradation of methylene blue under visible light. **Meriem Henni** application of the antibacterial activity of the synthesized materials; **Leila Djahnit** conservation of antibacterial activity data. **Maroua Bouzegaou** synthesis of material.

Conflicts of Interest

The authors declare no conflict of interest.

References

1 Maksoud, T. M. A., El-Sayed, H. A., & Ahmed, H. B. (2019). Antibacterial activity of metal oxide nanoparticles: A review. *Journal of Nanomaterials and Molecular Nanotechnology, 8*(2), 1–12. https://doi.org/10.4172/2324-8777.1000178

2 Soualmi, S., Djahnit, L., Henni, M., & Douar, R. (2025). Green synthesis of $ZnMn_2O_4$ nanoparticles using tragacanth gel for antibacterial effects. *Chemical Papers*, 1–14. https://doi.org/10.1007/s11696-025-04065-w.

3 Soualmi, S., Henni, M., Djahnit, L., & Hamdani, H. (2024). Sol-gel synthesized ZnO–$SrMn_2O_4$ nanocomposite and its antibacterial properties. *Eurasian Journal of Chemistry, 29*(4), 71–81. https://doi.org/10.31489/2959-0663/4-24-12

4 Fort, S., Hu, H., & Lakshminarayanan, B. (2019). Deep ensembles: A loss landscape perspective. *arXiv*. https://doi.org/10.48550/arXiv.1912.02757.

5 Heiba, Z. K., Ghannam, M. M., Badawi, A., & Mohamed, M. B. (2024). Tailoring the structure, optical and shielding characteristics of $ZnMn_2O_4$ nanostructures through Sn-doping. *ECS Journal of Solid State Science and Technology, 13*(7), 077001. doi: 10.1149/2162-8777/ad5b86.

6 Heiba, Z. K., Ghannam, M. M., Mohamed, M. B., Sanad, M. M. S., Abdel-Kader, M. H., El-Naggar, A. M., & Lakshminarayana, G. (2023). Impact of Bi doping on the structural, optical, and dielectric features of nano $ZnMn_2O_4$. *Ceramics International, 11*, 303. https://doi.org/10.1016/j.ceramint.2023.11.303.

7 Heiba, Z. K., Ghannam, M. M., Mohamed, M. B., Sanad, M. M., El-Naggar, A. M., & Shaltout, A. A. (2024). Influence of Al doping on the structural, optical, and electrical characteristics of $ZnMn_2O_4$. *ECS Journal of Solid State Science and Technology, 13*(2), 023008. https://doi.org/10.1149/2162-8777/ad28ca

8 Zhu, X., Quan, J., Huang, J., Ma, Z., Chen, Y., Zhu, D., & Li, D. (2018). A new approach to improve the electrochemical performance of $ZnMn_2O_4$ through a charge compensation mechanism using the substitution of Al^{3+} for Zn^{2+}. *RSC Advances, 8*(14), 7361–7368. https://doi.org/10.1039/c8ra00310f

9 Rajesh, G., Kumar, P. S., Alanazi, A. K., Rangasamy, G., & Abo-Dief, H. M. (2023). Development of lattice defects and oxygen vacancies in Zn-doped $CdAl_2O_4$ nanoparticles for improving the photocatalytic efficiencies of brilliant green and brilliant blue dyes under visible illumination. *Catalysis Communications, 183*, 106762. https://doi.org/10.1016/j.catcom.2023.106762

10 Ma, L., Wei, Z., Zhu, X., Liang, J., & Zhang, X. (2019). Synthesis and photocatalytic properties of Co-doped $Zn_{1-x}Co_xMn_2O$ hollow nanospheres. *Journal of Nanomaterials, 20*19, 4257270. https://doi.org/10.1155/2019/4257270

11 Ramon, M. V., Stoeckli, F., Moreno-Castilla, C., & Carrasco-Marin, F. (1999). On the characterization of acidic and basic surface sites on carbons by various techniques. *Carbon, 37*, 1215–1221. https://doi.org/10.1016/S0008-6223(98)00317-0

12 Imran, M., Riaz, S., Sanaullah, I., Khan, U., Sabri, A. N., & Naseem, S. (2019). Microwave assisted synthesis and antimicrobial activity of Fe_3O_4-doped ZrO_2 nanoparticles. *Ceramics International, 45*(8), 10106–10113. https://doi.org/10.1016/j.ceramint.2019.02.057

13 Roy, A., Ghosh, M., Ramos Ramón, J. A., Saha, S., Pal, U., & Das, S. (2019). Study on charge storage mechanism in working electrodes fabricated by sol-gel derived spinel $NiMn_2O_4$ nanoparticles for supercapacitor application. *Applied Surface Science, 463*, 513–525. https://doi.org/10.1016/j.apsusc.2018.08.259

14 Bond, G. C. (2005). Small metal particles and supported metal catalysts. In *Metal Catalysed Reactions of Hydrocarbons* (pp. 35–91). Elsevier. https://doi.org/10.1007/0-387-26111-7_2

15 Heiba, Z. K., Mohamed, M. B., & Badawi, A. (2022). Structural and optical properties of $(1-x)ZnMn_2O_4/x$PbS. *Journal of Materials Science: Materials in Electronics, 33*(14), 11354–11364.

16 Ma, Z., Ren, F., Ming, X., Long, Y., & Volinsky, A. A. (2019). Cu-doped ZnO electronic structure and optical properties studied by first principles calculations and experiments. *Materials, 12*(1), 196. https://doi.org/10.3390/ma12010196

17 Khalid, A., Ahmad, P., Alharthi, A. I., Muhammad, S., Khandaker, M. U., Rehman, M., & Bradley, D. A. (2021). Structural, optical, and antibacterial efficacy of pure and zinc doped copper oxide against pathogenic bacteria. *Nanomaterials, 11*(2), 293. https://doi.org/10.3390/nano11020451

18 Yıldırım, M. (2019). Characterization of the framework of Cu-doped TiO_2 layers: An insight into optical, electrical and photodiode parameters. *Journal of Alloys and Compounds, 773*, 890–904. https://doi.org/10.1016/j.jallcom.2018.09.276

19 Ali, B. M., Siddig, M. A., Alsabah, Y. A., Elbadawi, A. A., & Ahmed, A. I. (2018). Effect of Cu^{2+} doping on structural and optical properties of synthetic $Zn_{0.5}Cu_xMg_{0.5-x}Fe_2O_4$ ($x = 0.0$–0.4) nano ferrites. *Advances in Nanoparticles, 7*(1), 1–13. https://doi.org/10.4236/anp.2018.71001

20 Gherbi, R., Bessekhouad, Y., & Trari, M. (2016). Optical and transport properties of Sn-doped $ZnMn_2O_4$ prepared by sol–gel method. *Journal of Physics and Chemistry of Solids, 89*, 69–77. https://doi.org/10.1016/j.jpcs.2015.10.019

21 Lima, D. S., Gullon, B., Cardelle-Cobas, A., Brito, L. M., Rodrigues, K. A., Quelemes, P. V., ... & Batziou, K. (2017). Chitosan-based silver nanoparticles: A study of the antibacterial, antileishmanial and cytotoxic effects. *Journal of Bioactive and Compatible Polymers, 32*(4), 397–410. https://doi.org/10.1177/0883911516681329

22 Bogdanović, U., Lazić, V., Vodnik, V., Budimir, M., Marković, Z., & Dimitrijević, S. (2014). Copper nanoparticles with high antimicrobial activity. *Materials Letters, 128*, 75–78. https://doi.org/10.1016/j.matlet.2014.04.106

23 Giannousi, K., Lafazanis, K., Arvanitidis, J., Pantazaki, A., & Dendrinou-Samara, C. (2014). Hydrothermal synthesis of copper-based nanoparticles: Antimicrobial screening and interaction with DNA. *Journal of Inorganic Biochemistry, 133*, 24–32. https://doi.org/10.1016/j.jinorgbio.2013.12.009

24 Cai, Y., Stromme, M., Melhus, A., Engqvist, H., & Welch, K. (2013). Photocatalytic inactivation of biofilms on bioactive dental adhesives. *Journal of Biomedical Materials Research Part B: Applied Biomaterials, 102*, 62–67. https://doi.org/10.1002/jbm.b.32980

25 Kim, J., Cho, H., Ryu, S., & Choi, M. (2000). Effects of metal ions on the activity of protein tyrosine phosphatase VHR: Highly potent and reversible oxidative inactivation by Cu^{2+} ion. *Archives of Biochemistry and Biophysics, 382*, 72–80. https://doi.org/10.1006/abbi.2000.1996

26 Stohs, S. J., & Bagchi, D. (1995). Oxidative mechanisms in the toxicity of metal ions. *Free Radical Biology and Medicine, 18*, 321–336. https://doi.org/10.1016/0891-5849(94)00159-h

27 Park, G. D., Kang, Y. C., & Cho, J. S. (2022). Morphological and electrochemical properties of $ZnMn_2O_4$ nanopowders and their aggregated microspheres prepared by simple spray drying process. *Nanomaterials, 12*(4), 680. https://doi.org/10.3390/nano12040680